PHYSICAL REVIEW B **110**, L041201 (2024)

Letter

Indirect-to-direct band gap transition induced by *d*-*d* coupling between cations in rare-earth chalcogenide perovskites

Han Zhang,[1,2] Yichun Pan,[3] Zexin Liu,[3] Biao Zeng,[1,2] Xiaowei Wu,[1,2] Chen Ming,[1,2] Guoqing Xin,[3]
Weihang Zhou,[3] Hao Zeng,[4] Shengbai Zhang,[5] and Yi-Yang Sun[1,2,*]
[1]*State Key Laboratory of High Performance Ceramics and Superfine Microstructure, Shanghai Institute of Ceramics,
Chinese Academy of Sciences, Shanghai 201899, China*
[2]*Center of Materials Science and Optoelectronics Engineering, University of Chinese Academy of Sciences, Beijing 100049, China*
[3]*Wuhan National High Magnetic Field Center and School of Physics, Huazhong University of Science and Technology,
Wuhan, Hubei 430074, China*
[4]*Department of Physics, University at Buffalo, The State University of New York, Buffalo, New York 14260, USA*
[5]*Department of Physics, Applied Physics and Astronomy, Rensselaer Polytechnic Institute, Troy, New York 12180, USA*

(Received 12 October 2023; revised 6 July 2024; accepted 9 July 2024; published 25 July 2024)

Chalcogenide perovskite materials have been shown to exhibit excellent properties for optoelectronics and photovoltaics. The research, however, has been focused on the II-IV-S_3 series of compounds. Here, by theoretical calculation, we predict that in the III-III-S_3 perovskites, there could exist a transition between the indirect and direct band gaps induced by the coupling strength of the *d* orbitals between the A-site and B-site cations. We validate this prediction by synthesizing $LaScS_3$ through solid state reaction from three elemental materials. Micro-Raman analysis combined with Raman tensor calculations are used to identify the perovskite phase of micrometer-size grains, from which photoluminescence can be observed. The emitted light peaks at about 519 nm (or 2.39 eV), which corresponds to the largest band gap among the sulfide perovskites. The discovery of light-emitting $LaScS_3$ enriches the family of chalcogenide perovskites for optoelectronic applications.

DOI: 10.1103/PhysRevB.110.L041201

Semiconductor light-emitting devices have revolutionized various aspects of modern life. White light-emitting diodes (LEDs) [1–3] are rapidly replacing traditional devices like incandescent lamps, making significant strides in the lighting market. From mobile devices to theater-size screens, display technology is also increasingly adopting LEDs [4]. Semiconductor lasers [5], with their compact design, have facilitated a wide range of applications, including laboratory light sources, fiber optic communication [6], and autonomous driving [7]. However, despite these successful applications, there are still unresolved issues in the field of LEDs that necessitate the development of new optoelectronic materials and devices. For instance, the next-generation display technology, micro-LED, experiences efficiency deterioration in the red-color range when the device size shrinks below 20 μm [8]. Green-color LEDs often suffer from low quantum efficiency, creating what is commonly known as the "green gap" problem [9] when compared to blue-color and red-color LEDs. Furthermore, the long-term stability of recently developed halide perovskite LEDs, particularly the blue-color ones, remains a challenge due to the segregation of Cl and Br anions under working conditions [10–12].

Sulfide perovskites, a new family of optoelectronic materials, were initially proposed for photovoltaic applications [13], but they also display appealing luminescent properties. In a recent study by Kota *et al.*, $SrHfS_3$ was investigated and found to hold great potential as a green-color luminescent material [14]. In comparison to halide perovskites, sulfide perovskites possess inherent advantages such as thermal and environmental stability [15–18], as well as being free from toxic elements like lead [13]. However, research on sulfide perovskites has predominantly focused on the II-IV-S_3 series, composed of group-II elements (Ca, Sr, and Ba) and group-IV elements (Zr and Hf) [14–36]. The experimentally measured and theoretically calculated band gaps of these materials fall below 2.32 eV [13]. In our recent theoretical study, we predicted that the III-III-S_3 perovskite $YScS_3$ could possess a band gap approaching 3 eV. Unfortunately, its indirect nature renders it unsuitable for optoelectronic applications [37].

In this Letter, we draw inspiration from the wide band gap of $YScS_3$ and the recent discovery of $LaScSe_3$ [38], a predicted direct-gap selenide perovskite, to investigate the III-III-S_3 perovskite $LaScS_3$. Our objective is to discover novel optoelectronic materials. Through first-principles calculations, we find that the bottom of the conduction band in III-III-S_3 perovskites is primarily influenced by the *d*-*d* coupling between the A-site cation and B-site cation. In $YScS_3$, the strong coupling between the 4*d* orbitals of Y and 3*d* orbitals of Sc significantly lowers the band at the S point in the Brillouin zone, resulting in an indirect band gap. However, in $LaScS_3$, the coupling between the 5*d* orbitals of La and 3*d* orbitals of Sc is weaker than the 4*d*-3*d* coupling in $YScS_3$. As a result, the band at the S point is lifted, leading to a direct band gap in $LaScS_3$. To validate this theoretical prediction, we

---

[*] Contact author: yysun@mail.sic.ac.cn

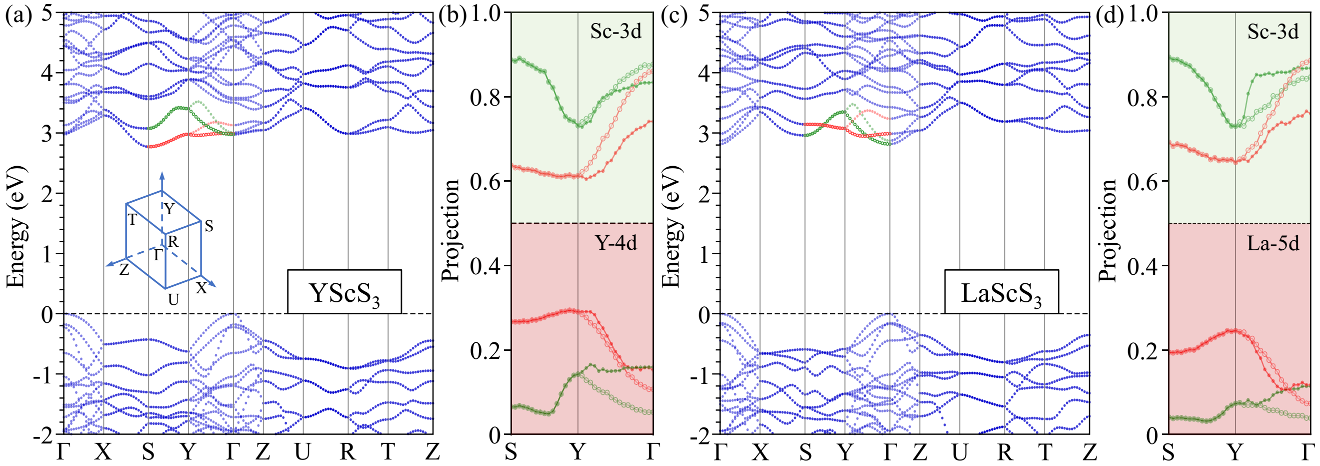

FIG. 1. (a), (c) show the band structures of YScS$_3$ and LaScS$_3$ based on HSE06 functional calculations. The inset shows the irreducible Brillouin zone. (b), (d) show the projection of bottom four conduction bands, as highlighted in (a), (c), on the *d* orbitals of A-site and B-site cations along the S-Y-Γ path for YScS$_3$ and LaScS$_3$, respectively.

synthesize LaScS$_3$ by solid-state reaction. Photoluminescence measurements, assisted by micro-Raman measurements and DFT calculations on Raman tensors, confirm our prediction that LaScS$_3$ exhibits a direct band gap. Our work thus expands the family of chalcogenide perovskites to the III-III-S$_3$ series for optoelectronic applications.

First-principles calculations in this work were based on density functional theory (DFT), as implemented in the VASP program [39]. Projector augmented wave (PAW) potentials [40] were used to describe the interaction between ion cores and valence electrons. The wave functions were expanded by plane-wave basis sets. Hierarchical exchange-correlation functionals were used in our calculations for different purposes: (1) PBEsol functional [41] was used in calculation of dielectric tensors; (2) strongly constrained and appropriately normed (SCAN) functional [42] was used in all structure relaxations and frequency calculations; (3) hybrid HSE06 functional [43] was used in band structure calculations, where the screening parameter for range separation was set to 0.2 Å^{-1} and the mixing parameter for Hartree-Fock exchange was set to 0.25. Raman tensors (α_{ij}^k) were calculated by the partial difference of dielectric tensor (ϵ_{ij}) with respect to the phonon modes ($\boldsymbol{q}^k$) at the Brillouin zone center according to $\alpha_{ij}^k = \frac{\partial \epsilon_{ij}}{\partial \boldsymbol{q}^k}$ [44]. The dielectric tensors were calculated using density functional perturbation theory [45]. More calculation details about Raman intensity, convergence criteria and *k*-point sampling in different parts of calculations are listed in the calculation method part and Tables S1 and S2 in the Supplementary Material (SM) [46].

Crystal structures of the synthesized samples were evaluated using x-ray diffraction (XRD, Bruker D8 Advance) with Cu K$_\alpha$ radiation, a tube current of 40 mA, and a tube voltage of 40 kV. The surface morphology and chemical composition were examined by scanning electron microscopy (SEM, Hitachi S-4800) and energy-dispersive spectroscopy (EDS, Hitachi S-4800). The photoluminescence and Raman measurements were conducted using three wavelengths for the excitation light. The system excited by the 360-nm laser is equipped with a Horiba iHR-550 spectrometer, while the system excited by the 473-nm and 532-nm lasers is equipped with a Renishaw inVia confocal Raman microscope.

Figure 1 shows the band structures of YScS$_3$ and LaScS$_3$ computed using the hybrid HSE06 functional. For comparison, Fig. S1 in the SM [46] also shows the band structures calculated with the SCAN and PBEsol functionals. The atomic structures, including lattice constants and internal parameters, were optimized using the SCAN functional (see Table S3 in the SM [46]). The band structures calculated with the three functionals exhibit similar features around the band edges, with YScS$_3$ exhibiting indirect bandgaps and LaScS$_3$ exhibiting direct band gaps. We also examine the effect of spin-orbit coupling (SOC) on the band structure. The results from calculations using HSE06 functional with SOC are shown in Fig. S2 in the SM [46]. We found that in LaScS$_3$, bands located approximately 1.5 eV above the conduction band minimum exhibit splitting, while the band structure of YScS$_3$ remains largely unchanged. Based on the results above, we conclude that the direct or indirect nature of LaScS$_3$ and YScS$_3$ is not affected by the exchange-correlation functional and the SOC effect.

To analyze the origin of the difference between the two materials, we focus on the bottom four bands along the S-Y-Γ direction, which are highlighted by red and green colors in Figs. 1(a) and 1(c). Note that from S to Y points, the bands are doubly degenerate. However, the point group symmetry cannot afford double degeneracy. As the 20-atom *Pnma* unit cell is derived from four five-atom *Pm*$\bar{3}$*m* unit cells by octahedron rotation, this process could result in legacy degeneracy from the high-symmetry cubic cell.

In Figs. 1(b) and 1(d), we plot the projections of each state on the *d* orbitals of A-site and B-site cations. It is seen that the green bands are dominated by Sc 3*d* orbitals. In contrast, the red bands contain more contributions from the Y 4*d* and La 5*d* orbitals, especially along the S-Y direction. For YScS$_3$, the projections of Y 4*d* orbitals on the red bands are 0.31 at the S point and 0.14 and 0.19 at the Γ point, respectively. For LaScS$_3$, the corresponding projections of La 5*d* orbitals are 0.24 at the S point and 0.09 and 0.14 at the Γ point, respectively. We also examine the effect of using different functionals on the projection values of the *d*-orbitals for the corresponding four bands. As shown in Fig. S3 in the SM [46], taking the S point as an example, the projection values of the *d*-orbitals for the corresponding four bands obtained using the HSE06, SCAN, and PBEsol functionals exhibit the same trend. Besides the smaller projections of La 5*d* orbitals, it is also expected that the coupling strength between the 5*d* and 3*d* orbitals is weaker than that between the 4*d* and 3*d* orbitals because of the larger energy level difference. The weaker 5*d*-3*d* coupling in $LaScS_3$ render the red bands along the S-Y direction lifted up so that the band gap becomes direct at the Γ point. According to the HSE06 calculation, the direct band gap of $LaScS_3$ is 2.81 eV.

Note that the effect of *d*-*d* coupling discussed above is entangled with the effect of atomic structure difference between the two materials, e.g., the octahedral titling. In the case of cubic $LaScS_3$ without any octahedral tilting, its band gap is indirect and the band gap value is also significantly smaller (see Fig. S4 in the SM [46]). Table S3 in the SM [46] compares the atomic structures of $LaScS_3$ and $YScS_3$, including the octahedral titling angles. It is found that $YScS_3$ exhibits larger titling angles than $LaScS_3$, which also influence the band structures. Figure S5 in the SM [46] compares the band structures of $LaScS_3$ with the octahedra in the native tilting angles and in the angles of $YScS_3$. It is seen that the tilting angles have a similar effect of shifting the red bands near the bottom conduction bands. Thus, from the atomic structure point of view, the octahedral titling contributes to the indirect-to-direct transition, while from the electronic structure point of view, the $d-d$ coupling plays an important role in this transition.

To validate the prediction above, we synthesize $LaScS_3$ by solid-state reaction. Up to date, only two papers reported the synthesis of $LaScS_3$ [47,48], where the binary sulfides were first synthesized and used as the reactants to obtain the ternary compound. Here, we use elemental La (purity 99.9% from Alfa), Sc (purity 99.9% from Alfa), and S (purity 99.998% from Aldrich) as reactants to obtain $LaScS_3$. The elemental reactants were weighed, put in an Al_2O_3 crucible, and then sealed in a quartz tube within an Ar-filled glovebox. The mixture was heated in a muffle furnace at 1100° C for 72 hours. The resulting product was grounded, pressed into a pellet, and resealed in a quartz tube within the glovebox. Then, the pellet was heated again at 1100° C for 72 hours.

Figure 2(a) displays the XRD pattern of the obtained $LaScS_3$ powder. We compared the experimental pattern with that calculated based on the structure optimized using the SCAN functional. The good agreement between the two patterns indicates the successful synthesis of a pure phase of $LaScS_3$, up to the detection limit of our XRD equipment. Moreover, this comparison highlights the high accuracy of the computationally optimized structure using the SCAN functional. In Fig. 2(a), we also compared the XRD patterns of our experiment and that from the structure listed in the ICSD, which is linked to in a previous reference [48]. The obtained reliability factor R_p (0.105) using the ICSD structure is slightly worse than the R_p (0.071) obtained using our optimized structure. The formula for evaluating R_p [49,50] is provided in the SM [46].

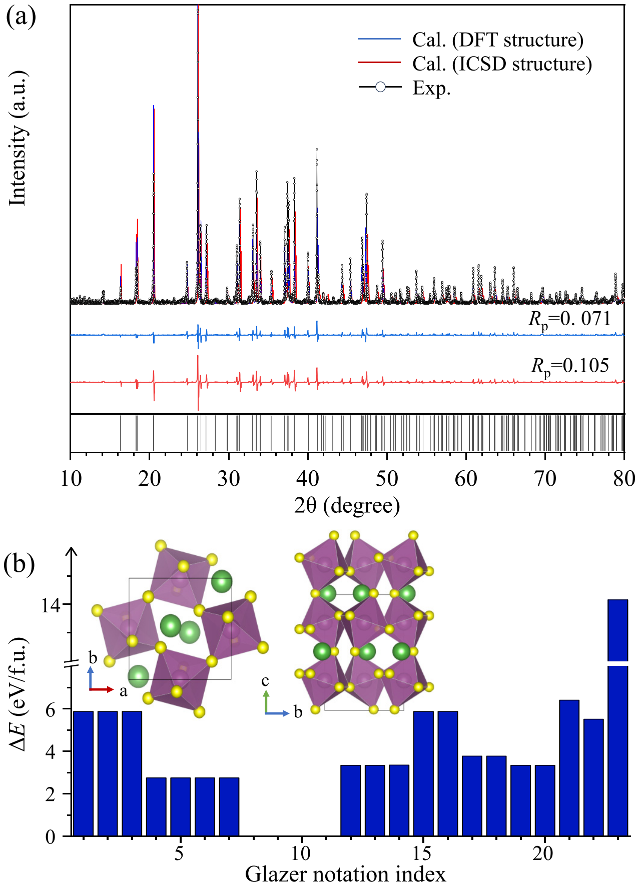

FIG. 2. (a) XRD pattern of powder $LaScS_3$ sample compared with calculated patterns using the atomic structures obtained from the SCAN functional calculation and the ICSD database. The red and blue lines below the patterns show the differences between the experimental and calculated patterns. Corresponding reliability factors (R_p) are also shown together with the lines. The black short lines at the bottom display the XRD peak positions calculated using the atomic structure obtained from the SCAN functional. (b) Calculated total energy of $LaScS_3$ with 23 different octahedron rotation patterns following the Glazer notation based on the SCAN functional, where the lowest energy patterns are taken as the energy reference. The inset shows the structure with the lowest total energy, which possesses the *Pnma* space-group symmetry (No. 62).

The space group symmetry of $LaScS_3$ has been labeled as *Pna*21 (No. 33) in the ICSD with the Sc atoms displaced away from the octahedron centers. However, our DFT calculations using the SCAN functional yielded a higher symmetry with space group *Pnma* (No. 62). Additionally, as shown in Fig. S6 in the SM [46], the phonon spectrum of $LaScS_3$ calculated using the SCAN functional did not exhibit any imaginary frequencies, indicating that the *Pnma* structure is stable. As seen in Fig. 2(a), our high-symmetry structure also yielded smaller R_p factor, suggesting that the actual structure of $LaScS_3$ has the *Pnma* symmetry. Similar symmetry issue also occurred for $CeScS_3$, which was reported to have a lower symmetry and then redetermined to be the *Pnma* symmetry [51,52]. In addition, we measured the ferroelectric properties of $LaScS_3$ by fabricating a ceramic plate using spark plasma sintering. The result is presented in Fig. S7 in the SM [46] and suggests

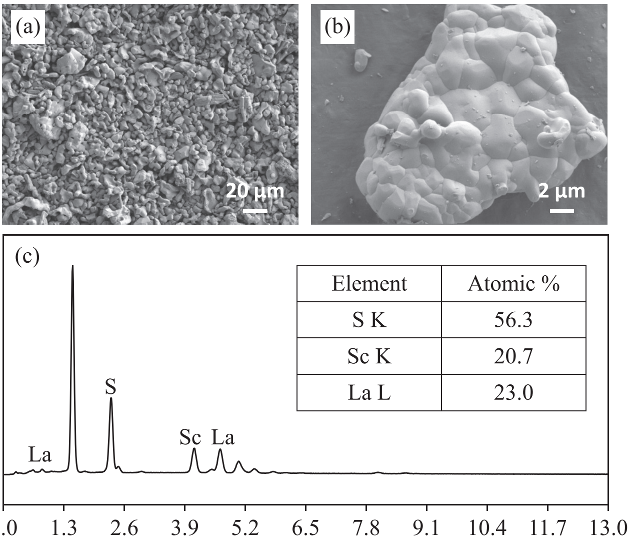

Element	Atomic %
S K	56.3
Sc K	20.7
La L	23.0

FIG. 3. SEM images of the synthesized $LaScS_3$ sample magnified by (a) 500 and (b) 5000 times and (c) EDS spectrum acquired from the sample in (b). The table of the inset lists the atomic ratio of the La, Sc, and S elements determined from the EDS measurement.

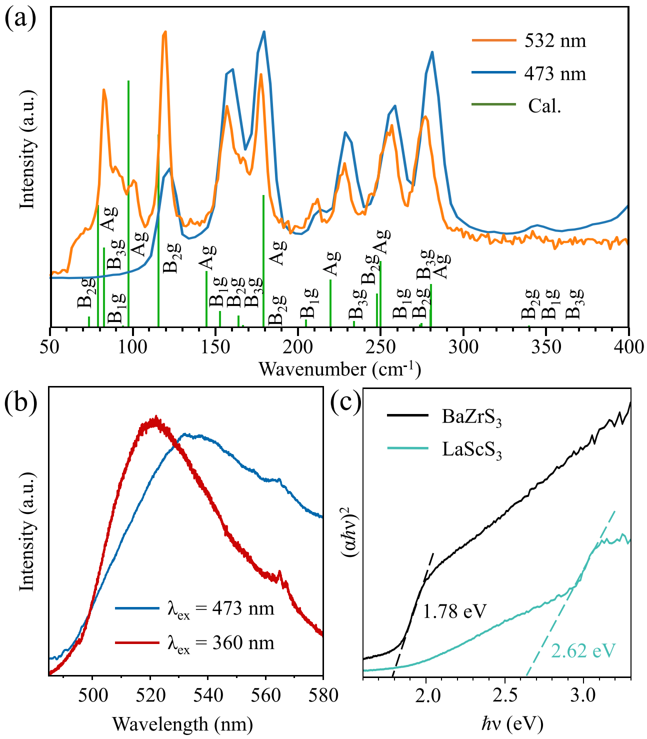

FIG. 4. (a) Raman spectra of $LaScS_3$ obtained using laser wavelengths of 532 nm and 473 nm. The calculated Raman peak positions and intensities, as well as the symmetry labels, are shown for comparison. (b) PL spectra of $LaScS_3$ using excitation laser wavelengths of 473 nm and 360 nm. (c) Optical absorption spectra of $LaScS_3$ and $BaZrS_3$ from diffuse reflectance spectroscopy.

that the material lacks ferroelectricity. Based on the results above, we conclude that $LaScS_3$ has the *Pnma* perovskite structure.

We also carried out a systematic determination of the particular octahedron rotation pattern in the perovskite structure by employing the Glazer notation [53], which classified the octahedron rotations into 23 possibilities. The information on the space groups of the 23 possible structures and their corresponding rotation modes is displayed in Table S4 in the SM [46]. In these calculations, we employed a supercell containing eight octahedra (i.e., a 2×2×2 supercell based on the nondistorted cubic perovskite unit cell) to accommodate the alternating octahedron rotations between nearest neighbors. The SCAN functional [42] and a 4×4×4 k-mesh were employed in these calculations to ensure computational accuracy. Figure 2(b) shows the calculated total energies with respect to the most stable rotation pattern. After relaxation, the patterns from 8 to 11, namely, $a^+b^-c^-$, $a^+a^-c^-$, $a^+b^-b^-$, and $a^+a^-a^-$, all ended up with the *Pnma* symmetry, which is the lowest-energy structure. The energy difference among the four patterns is less than 2 meV per formula of $LaScS_3$. Additionally, a 6×6×6 k-mesh was used to check the convergence of the energy, and the results are presented in Table S5 in the SM [46]. For comparison, we also performed the above calculations using the PBEsol functional [41], as shown in Fig. S8 in the SM [46]. The calculated results are consistent with the trends based on the SCAN functional, where the energy of patterns from 8 to 11 is the lowest, exhibiting the symmetry of *Pnma*.

Scanning electron microscope (SEM) characterization was conducted on the as-synthesized $LaScS_3$ powder samples. At a magnification of 500×, displayed in Fig. 3(a), grains of various sizes can be observed. At a magnification of 5000×, displayed in Fig. 3(b), detailed structure of a single grain can be observed to be polycrystalline with the grain boundaries clearly seen. By performing selected area electron diffraction (SAED) on the grains and calibrating the diffraction patterns, it can be demonstrated that the grains within the grain boundaries are single crystals. The characterization results are shown in Fig. S9 in the SM [46]. Energy-dispersive x-ray spectroscopy (EDS) was used to measure the chemical composition. An elemental ratio of approximately 1:1:3 was obtained for La:Sc:S, as shown in Fig. 3(c). The results of the EDS mapping are presented in Fig. S10 in the SM [46], indicating uniform elemental distribution in the prepared material. Additionally, a very small amount of black impurity grains were observed in the SEM analysis. According to the EDS results, the elemental composition of these impurity grains is approximately Sc:Si:O = 2:2:7. The results of the EDS analysis are presented in Fig. S11 in the SM [46].

We performed micro-Raman spectroscopy on individual polycrystalline grains. Continuous-wave lasers of 473 nm and 532 nm were used as the light source. As shown in Fig. 4(a), we obtained consistent Raman spectra, with Raman signals detected even below 110 cm^{-1} for the 532-nm excitation. To analyze the Raman spectra, we calculated the Raman tensors of $LaScS_3$ using the SCAN functional, from which the theoretical peak intensity can be estimated. As shown in Fig. 4(a), the calculated and the experimental spectra are in good agreement considering possible errors of about 10 cm^{-1} in the calculated peak positions, and symmetry labels were assigned to all Raman active peaks, as labeled in red. The calculation results of all Raman active modes are provided in the Table S6 in the SM [46].

The micro-Raman spectroscopy using the 473-nm laser allows us to measure the Raman and photoluminescence (PL) spectra on the same grain so that we can exclude the possibility that the PL signal is from an impurity grain. As shown in Fig. 4(b), a PL peak at 530 nm was observed. PL spectra of $LaScS_3$ were also measured using a 360-nm laser and a peak at 519 nm was observed, which corresponds to a band gap of 2.39 eV. We also performed diffuse reflectance spectroscopy (DRS) measurements. By the Tauc plot of the spectrum, as shown in Fig. 4(c), the direct band gap is approximately determined to be 2.62 eV. We compared with $BaZrS_3$, for which the direct band gap is found to be 1.78 eV, consistent with most reported values in the literature [24,32]. The discrepancy on the band gap values from our HSE06 calculation, PL and DRS measurements could be originated from the excitonic effect excluded from our DFT calculation and the inaccurate treatment of the localized La $4f$ and Sc $3d$ orbitals in the conduction band. The quality of the powder sample may also contribute the discrepancy, which calls for further study to investigate.

It is worth noting that the powder samples used in micro-Raman measurement were dispersed in alcohol using 100-Hz ultrasonic treatment for 10 minutes, transferred to glass slides, and then dried before the measurements. The Raman spectra obtained from alcohol-dispersed samples and those obtained without alcohol dispersion showed good consistency, as shown in Fig. S12 in the SM [46]. All measurements were performed under ambient conditions, demonstrating the good stability of the $LaScS_3$ perovskite.

In summary, by density functional theory calculation we predicted a light-emitting III-III-S_3 perovskite material, $LaScS_3$. The direct band gap can be attributed to the relatively weak coupling between the La $5d$ orbitals and Sc $3d$ orbitals. We synthesized $LaScS_3$ through solid-state reaction from the three elemental materials. Combining micro-Raman and PL spectrum measurements, we verified the theoretical prediction by observing PL spectrum peaking at 519 nm, which is in reasonable agreement with the theoretical value and indicates the largest band gap among the chalcogenide perovskites. As the first light-emitting III-III-S_3 perovskite, $LaScS_3$ expands the choices of chalcogenide perovskites and, indeed, the entire perovskite family, for optoelectronic applications.

The authors thank Zhen Liu, Xiangchao Kong, and Biao He for their help on ferroelectric property measurements. This work is supported by the National Key Research and Development Program of China under Grant No. 2021YFB3500501. Y.-Y.S. acknowledges the support from the National Natural Science Foundation of China under Grant No. 91963208. C.M. acknowledges the support from the Natural Science Foundation of Shanghai under Grant No. 23ZR1472500. H.Z. acknowledges the support from NSF under Grant No. DMR-2042085. S.Z. acknowledges the support from NSF under Grant No. DMR-2042126.

---

[1] S. Nakamura, T. Mukai, and M. Senoh, Candela-class high-brightness InGaN/AlGaN double-heterostructure blue-light-emitting diodes, Appl. Phys. Lett. **64**, 1687 (1994).

[2] S. Nakamura, M. Senoh, N. Iwasa, S.-I. Nagahama, T. Yamada, and T. Mukai, Superbright green InGaN single-quantum-well-structure light-emitting diodes, Jpn. J. Appl. Phys. **34**, L1332 (1995).

[3] G. Blasse and A. Bril, A new phosphor for flying-spot cathode-ray tubes for color television: Yellow-emitting $Y_3Al_5O_{12}$-Ce^{3+}, Appl. Phys. Lett. **11**, 53 (1967).

[4] X. Lv, K. H. Loo, Y. M. Lai, and C. K. Tse, Energy-saving driver design for full-color large-area led display panel systems, IEEE Trans. Ind. Electron. **61**, 4665 (2014).

[5] D. Welch, A brief history of high-power semiconductor lasers, IEEE J. Select. Topics Quantum Electron. **6**, 1470 (2000).

[6] H. Kressel, M. Ettenberg, J. P. Wittke, and I. Ladany, Laser diodes and LEDs for fiber optical communication, in *Semiconductor Devices for Optical Communication*, edited by H. Kressel, Topics in Applied Physics (Springer, Berlin, 1982), pp. 9–62.

[7] J. Y. Cho, K.-B. Kim, W. S. Hwang, C. H. Yang, J. H. Ahn, S. D. Hong, D. H. Jeon, G. J. Song, C. H. Ryu, S. B. Woo, J. Kim, T. H. Lee, J. Y. Choi, H. Cheong, and T. H. Sung, A multifunctional road-compatible piezoelectric energy harvester for autonomous driver-assist LED indicators with a self-monitoring system, Appl. Energy **242**, 294 (2019).

[8] Z. Chen, S. Yan, and C. Danesh, MicroLED technologies and applications: Characteristics, fabrication, progress, and challenges, J. Phys. D: Appl. Phys. **54**, 123001 (2021).

[9] M. Auf der Maur, A. Pecchia, G. Penazzi, W. Rodrigues, and A. Di Carlo, Efficiency drop in green InGaN/GaN light emitting diodes: The role of random alloy fluctuations, Phys. Rev. Lett. **116**, 027401 (2016).

[10] Z. Ren, K. Wang, X. W. Sun, and W. C. H. Choy, Strategies toward efficient blue perovskite light-emitting diodes, Adv. Funct. Mater. **31**, 2100516 (2021).

[11] L. Zhao, K. Roh, S. Kacmoli, K. Al Kurdi, S. Jhulki, S. Barlow, S. R. Marder, C. Gmachl, and B. P. Rand, Thermal management enables bright and stable perovskite light-emitting diodes, Adv. Mater. **32**, 2000752 (2020).

[12] Y. Zou, T. Wu, F. Fu, S. Bai, L. Cai, Z. Yuan, Y. Li, R. Li, W. Xu, T. Song, Y. Yang, X. Gao, F. Gao, and B. Sun, Thermal-induced interface degradation in perovskite light-emitting diodes, J. Mater. Chem. C **8**, 15079 (2020).

[13] K. V. Sopiha, C. Comparotto, J. A. Márquez, and J. J. S. Scragg, Chalcogenide perovskites: Tantalizing prospects, challenging materials, Adv. Opt. Mater. **10**, 2101704 (2022).

[14] K. Hanzawa, S. Iimura, H. Hiramatsu, and H. Hosono, Material design of green-light-emitting semiconductors: Perovskite-type sulfide $SrHfS_3$, J. Am. Chem. Soc. **141**, 5343 (2019).

[15] N. Gross, Y.-Y. Sun, S. Perera, H. Hui, X. Wei, S. Zhang, H. Zeng, and B. A. Weinstein, Stability and band-gap tuning of the chalcogenide perovskite $BaZrS_3$ in Raman and optical investigations at high pressures, Phys. Rev. Appl. **8**, 044014 (2017).

[16] T. Gupta, D. Ghoshal, A. Yoshimura, S. Basu, P. K. Chow, A. S. Lakhnot, J. Pandey, J. M. Warrender, H. Efstathiadis, A. Soni, E. Osei-Agyemang, G. Balasubramanian, S. Zhang, S.-F. Shi, T.-M. Lu, V. Meunier, and N. Koratkar, An environmentally stable and lead-free chalcogenide perovskite, Adv. Funct. Mater. **30**, 2001387 (2020).

[17] S. Niu, J. Milam-Guerrero, Y. Zhou, K. Ye, B. Zhao, B. C. Melot, and J. Ravichandran, Thermal stability study of transition metal perovskite sulfides, J. Mater. Res. **33**, 4135 (2018).

[18] Y. Wang, N. Sato, and T. Fujino, Synthesis of $BaZrS_3$ by short time reaction at lower temperatures, J. Alloys Compd. **327**, 104 (2001).

[19] C. Comparotto, A. Davydova, T. Ericson, L. Riekehr, M. V. Moro, T. Kubart, and J. Scragg, Chalcogenide perovskite $BaZrS_3$: Thin film growth by sputtering and rapid thermal processing, ACS Appl. Energy Mater. **3**, 2762 (2020).

[20] J. A. Márquez, M. Rusu, H. Hempel, I. Y. Ahmet, M. Kölbach, I. Simsek, L. Choubrac, G. Gurieva, R. Gunder, S. Schorr, and T. Unold, $BaZrS_3$ chalcogenide perovskite thin films by H_2S sulfurization of oxide precursors, J. Phys. Chem. Lett. **12**, 2148 (2021).

[21] W. Meng, B. Saparov, F. Hong, J. Wang, D. B. Mitzi, and Y. Yan, Alloying and defect control within chalcogenide perovskites for optimized photovoltaic application, Chem. Mater. **28**, 821 (2016).

[22] Y. Nishigaki, T. Nagai, M. Nishiwaki, T. Aizawa, M. Kozawa, K. Hanzawa, Y. Kato, H. Sai, H. Hiramatsu, H. Hosono, and H. Fujiwara, Extraordinary strong band-edge absorption in distorted chalcogenide perovskites, Solar RRL **4**, 1900555 (2020).

[23] S. Niu, H. Huyan, Y. Liu, M. Yeung, K. Ye, L. Blankemeier, T. Orvis, D. Sarkar, D. J. Singh, R. Kapadia, and J. Ravichandran, Bandgap control via structural and chemical tuning of transition metal perovskite chalcogenides, Adv. Mater. **29**, 1604733 (2017).

[24] S. Perera, H. Hui, C. Zhao, H. Xue, F. Sun, C. Deng, N. Gross, C. Milleville, X. Xu, D. F. Watson, B. Weinstein, Y.-Y. Sun, S. Zhang, and H. Zeng, Chalcogenide perovskites–an emerging class of ionic semiconductors, Nano Energy **22**, 129 (2016).

[25] A. A. Pradhan, M. C. Uible, S. Agarwal, J. W. Turnley, S. Khandelwal, J. M. Peterson, D. D. Blach, R. N. Swope, L. Huang, S. C. Bart, and R. Agrawal, Synthesis of $BaZrS_3$ and $BaHfS_3$ chalcogenide perovskite films using single-phase molecular precursors at moderate temperatures, Angew. Chem. Int. Ed. **62**, e202301049 (2023).

[26] V. K. Ravi, S. H. Yu, P. K. Rajput, C. Nayak, D. Bhattacharyya, D. S. Chung, and A. Nag, Colloidal $BaZrS_3$ chalcogenide perovskite nanocrystals for thin film device fabrication, Nanoscale **13**, 1616 (2021).

[27] I. Sadeghi, K. Ye, M. Xu, Y. Li, J. M. LeBeau, and R. Jaramillo, Making $BaZrS_3$ chalcogenide perovskite thin films by molecular beam epitaxy, Adv. Funct. Mater. **31**, 2105563 (2021).

[28] Y.-Y. Sun, M. L. Agiorgousis, P. Zhang, and S. Zhang, Chalcogenide perovskites for photovoltaics, Nano Lett. **15**, 581 (2015).

[29] M. Surendran, H. Chen, B. Zhao, A. S. Thind, S. Singh, T. Orvis, H. Zhao, J.-K. Han, H. Htoon, M. Kawasaki, R. Mishra, and J. Ravichandran, Epitaxial thin films of a chalcogenide perovskite, Chem. Mater. **33**, 7457 (2021).

[30] N. Thakur, P. Kumar, R. Neffati, and P. Sharma, Design and simulation of chalcogenide perovskite $BaZr(S, Se)_3$ compositions for photovoltaic applications, Phys. Scr. **98**, 065921 (2023).

[31] J. W. Turnley, K. C. Vincent, A. A. Pradhan, I. Panicker, R. Swope, M. C. Uible, S. C. Bart, and R. Agrawal, Solution deposition for chalcogenide perovskites: A low-temperature route to $BaMS_3$ materials ($M = Ti, Zr, Hf$), J. Am. Chem. Soc. **144**, 18234 (2022).

[32] X. Wei, H. Hui, C. Zhao, C. Deng, M. Han, Z. Yu, A. Sheng, P. Roy, A. Chen, J. Lin, D. F. Watson, Y.-Y. Sun, T. Thomay, S. Yang, Q. Jia, S. Zhang, and H. Zeng, Realization of $BaZrS_3$ chalcogenide perovskite thin films for optoelectronics, Nano Energy **68**, 104317 (2020).

[33] X. Wei, H. Hui, S. Perera, A. Sheng, D. F. Watson, Y.-Y. Sun, Q. Jia, S. Zhang, and H. Zeng, Ti-alloying of $BaZrS_3$ chalcogenide perovskite for photovoltaics, ACS Omega **5**, 18579 (2020).

[34] X. Wu, W. Gao, J. Chai, C. Ming, M. Chen, H. Zeng, P. Zhang, S. Zhang, and Y.-Y. Sun, Defect tolerance in chalcogenide perovskite photovoltaic material $BaZrS_3$, Sci. China Mater. **64**, 2976 (2021).

[35] R. Yang, A. D. Jess, C. Fai, and C. J. Hages, Low-temperature, solution-based synthesis of luminescent chalcogenide perovskite $BaZrS_3$ nanoparticles, J. Am. Chem. Soc. **144**, 15928 (2022).

[36] Z. Yu, X. Wei, Y. Zheng, H. Hui, M. Bian, S. Dhole, J.-H. Seo, Y.-Y. Sun, Q. Jia, S. Zhang, S. Yang, and H. Zeng, Chalcogenide perovskite $BaZrS_3$ thin-film electronic and optoelectronic devices by low temperature processing, Nano Energy **85**, 105959 (2021).

[37] H. Zhang, C. Ming, K. Yang, H. Zeng, S. Zhang, and Y.-Y. Sun, Chalcogenide perovskite $YScS_3$ as a potential p-type transparent conducting material, Chin. Phys. Lett. **37**, 097201 (2020).

[38] H. Zhang, X. Wu, K. Ding, L. Xie, K. Yang, C. Ming, S. Bai, H. Zeng, S. Zhang, and Y.-Y. Sun, Prediction and synthesis of a selenide perovskite for optoelectronics, Chem. Mater. **35**, 4128 (2023).

[39] G. Kresse and J. Furthmüller, Efficiency of ab-initio total energy calculations for metals and semiconductors using a plane-wave basis set, Comput. Mater. Sci. **6**, 15 (1996).

[40] G. Kresse and D. Joubert, From ultrasoft pseudopotentials to the projector augmented-wave method, Phys. Rev. B **59**, 1758 (1999).

[41] J. P. Perdew, A. Ruzsinszky, G. I. Csonka, O. A. Vydrov, G. E. Scuseria, L. A. Constantin, X. Zhou, and K. Burke, Restoring the density-gradient expansion for exchange in solids and surfaces, Phys. Rev. Lett. **100**, 136406 (2008).

[42] J. Sun, A. Ruzsinszky, and J. P. Perdew, Strongly constrained and appropriately normed semilocal density functional, Phys. Rev. Lett. **115**, 036402 (2015).

[43] J. Heyd, G. E. Scuseria, and M. Ernzerhof, Hybrid functionals based on a screened Coulomb potential, J. Chem. Phys. **118**, 8207 (2003), **124**, 219906 (2006).

[44] R. Caracas, Raman spectra and lattice dynamics of cubic gauche nitrogen, J. Chem. Phys. **127**, 144510 (2007).

[45] M. Gajdoš, K. Hummer, G. Kresse, J. Furthmüller, and F. Bechstedt, Linear optical properties in the projector-augmented wave methodology, Phys. Rev. B **73**, 045112 (2006).

[46] See Supplemental Material at http://link.aps.org/supplemental/10.1103/PhysRevB.110.L041201 for the computational method and details, band structures of $LaScS_3$ and $YScS_3$ calculated

by considering different functionals and spin-orbit coupling effect, phonon spectrum of $LaScS_3$, ferroelectric measurement on $LaScS_3$, selected area electron diffraction patterns, scanning electron microscopy images, energy-dispersive x-ray spectroscopy results, calculated Raman spectrum of $LaScS_3$, and stability study by Raman spectroscopy.

[47] O. V. Andreev, O. Yu. Mitroshin, and I. A. Razumkova, Phase diagrams of the systems $Sc_2S_3 - Ln_2S_3$ for Ln = La, Nd, or Gd, Russ. J. Inorg. Chem. **52**, 1161 (2007).

[48] R. Noel, L. Pierre, and F. Jean, Sur une nouvelle serie de combinaisons des sesquisulfures de terres rares et d'yttrium avec le sesquisulfure de scandium, C. R. Acad. Sci. Paris **269**, 1391 (1969).

[49] D. L. Bish and J. E. Post, *Modern Powder Diffraction* (Walter de Gruyter, Berlin, 1989).

[50] L. B. McCusker, R. B. Von Dreele, D. E. Cox, D. Louër, and P. Scardi, Rietveld refinement guidelines, J. Appl. Cryst. **32**, 36 (1999).

[51] K. J. Range, A. Gietl, and U. Klement, Crystal structure of cerium scandium trisulfide, $CeScS_3$, Z. Kristallogr. Cryst. Mater. **207**, 147 (1993).

[52] D. J. W. IJdo, Cerium scandium sulphide: Structure refinement by powder neutron diffraction, Acta Cryst. B **36**, 2403 (1980).

[53] A. M. Glazer, The classification of tilted octahedra in perovskites, Acta Cryst. B **28**, 3384 (1972).